Sub-organ Level Quantitation of Proteins in Tissues Delivered by Polymeric Nanocarriers

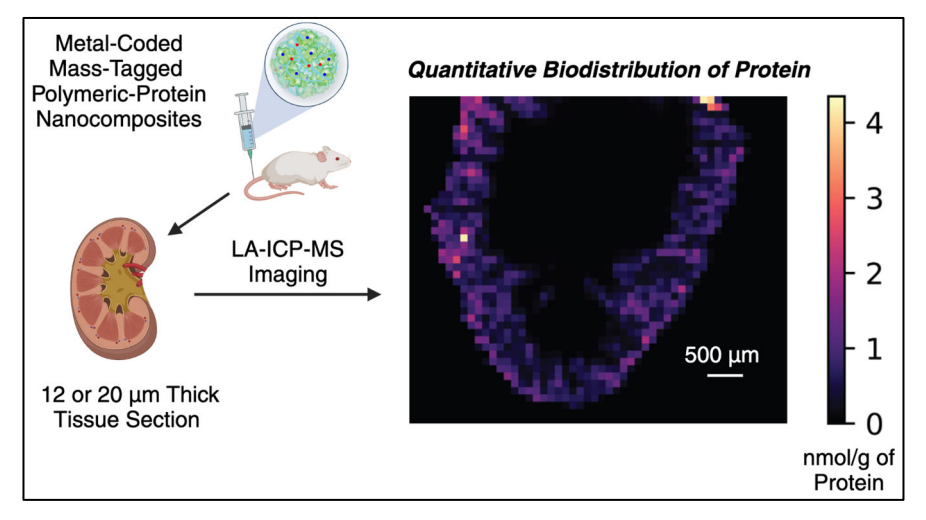
Dheeraj K. Agrohia,¹ Ritabrita Goswami,¹ Teerapong Jantarat,¹ Yağız Anil Çiçek,¹ Korndanai Thongsukh,¹ Taewon Jeon,² Jonathan M. Bell,¹ Vincent M. Rotello¹,² and Richard W. Vachet¹,²*

¹Department of Chemistry, University of Massachusetts Amherst, Amherst, MA 01003, USA
²Molecular and Cellular Biology Program, University of Massachusetts Amherst, Amherst, MA 01003, USA

Corresponding authors:

^{*}rwvachet@chem.umass.edu

ABSTRACT



Amidst the rapid growth of protein therapeutics as a drug class, there is an increased focus on designing systems to effectively deliver proteins to target organs. Quantitative monitoring of protein distributions in tissues is essential for optimal development of delivery systems; however, existing strategies can have limited accuracy, making it difficult to assess sub-organ dosing. Here, we describe a quantitative imaging approach that utilizes metal-coded mass tags and laser ablation inductively-coupled plasma mass spectrometry (LA-ICP-MS) to quantify the sub-organ distributions of proteins in tissues that have been delivered by polymeric nanocarriers. Using this approach, we measure nmol/g levels of proteins as delivered by guanidinium-functionalized poly(oxanorborneneimide) (PONI) polymers to various tissues, including the alveolar region of the lung. Due to the multiplexing capability of the LA-ICP-MS imaging, we are also able to simultaneously quantify protein and polymer distributions, obtaining valuable information about the relative excretion pathways of the protein cargo and carrier. This imaging approach will facilitate quantitative correlations between nanocarrier properties and protein cargo biodistributions.

Keywords: nanomaterials; imaging; mass spectrometry; quantitation; therapeutic delivery; polymer; inductively-coupled plasma

INTRODUCTION

Proteins have emerged as an important class of therapeutic agents, with more than 200 therapeutics having been approved by the FDA and even more in development.^{1,2} However, the failure rate for protein therapeutics vastly exceeds their success rate, which poses a significant challenge in the field.³ Vectors delivering protein therapeutics can overcome inherent challenges for protein therapeutics, including poor *in vivo* stability,^{4–6} limited half-lives,⁷ immunogenicity,^{8–10} and limited membrane permeability.^{11,12}

Nanocarriers can augment protein stability, mitigate immunogenicity risks, and enhance cellular uptake. ^{13–15} It is crucial to understand the spatial distributions of administered proteins to optimally develop potent nanocarrier-based protein therapies. ^{16,17} However, it is difficult to predict the *in vivo* fate, and hence potency, of nanocarriers, where localized delivery depends on many factors such as vector size, ¹⁸ charge, ^{19,20} shape, ²¹ and their *in vivo* identity arising from protein corona formation. ²² Tissue-specific measurements of protein therapeutic distributions among different cell types in targeted and non-targeted tissues can provide a measure of the efficacy of delivery systems. Sub-organ information in the liver and kidney, for example, provides insight into excretion mechanisms. ^{23,24} A method that can give site-specific quantitative information of protein therapeutics would yield dosing information to facilitate the development of potent and safe protein delivery systems.

Fluorescence microscopy and nuclear imaging are commonly used techniques to monitor protein therapeutics *in vivo*.²⁵ Fluorescence microscopy is widely used to monitor protein therapeutics because of its simplicity and high sensitivity.^{25–30} Numerous studies have used fluorescence imaging to track the delivery of protein therapeutics with systems ranging from lipid-based nanocarriers to metal and polymer-based nanocarriers.^{31–34} Nuclear imaging techniques such

as positron emission tomography (PET) and single photon emission computed tomography (SPECT) are increasingly used to track proteins *in vivo* via radioactive probes attached to the proteins of interest.^{35–39} Numerous studies have used nuclear imaging to study the biodistribution of protein therapeutics delivered by protein and polymer-based nanomaterials.^{40,41}

Despite the broad usage of fluorescence microscopy and nuclear imaging for tracking protein delivery, each faces challenges for obtaining quantitative data. Fluorescence imaging has inherent limitations such as quenching, intrinsic interferences, and limited multiplexing capability. 42-44 To advance the development of next-generation delivery vehicles, it is crucial to quantitatively track nanocarrier-associated cargos *in vivo*. Fluorescence signals are influenced by the local microenvironment of the fluorophore, and this characteristic can sometime lead to challenges in achieving absolute quantification in fluorescence imaging. 45 Nuclear imaging approaches also face challenges in quantification due to a variety of artifacts caused by the instrumentation and reconstruction algorithms that are used, resulting in the techniques being most commonly used for the relative quantitation of therapeutics in diseased vs. healthy tissues. 46 In addition, nuclear imaging techniques have stringent safety requirements, relatively modest spatial resolution (~ 1 mm), few readily available sources of radioisotopes, and a lack of broad accessibility to instrumentation. 44 Hence, better methods that can more readily quantitate protein therapeutics with higher spatial resolution in animals are needed.

Mass spectrometry imaging (MSI) is emerging as a versatile technique to analyze the site-specific biodistributions of proteins. Matrix-assisted laser desorption ionization (MALDI) MSI,^{47–50} desorption electrospray ionization (DESI) MSI,^{51–53} and imaging mass cytometry (IMC)^{54–57} can measure the spatial distributions of proteins in tissues. For all of these MSI methods, however, quantitative measures of protein levels are not readily achievable, mainly due to variations in

protein ionization efficiencies as in the case of MALDI-MSI and DESI-MSI and the lack of appropriate standards for IMC. Overall, quantitative imaging of protein therapeutics with suborgan spatial resolution is still difficult.

Here, we describe an approach that uses metal-coded mass tags (MMT)⁵⁸ together with laser ablation inductively-coupled-plasma (LA-ICP) MSI to site-specifically quantify proteins in tissues that have been delivered by polymeric nanocarrier systems (Figure 1). Guanidinium-functionalized poly(oxanorborneneimide) (PONI) polymers were used as a model delivery system

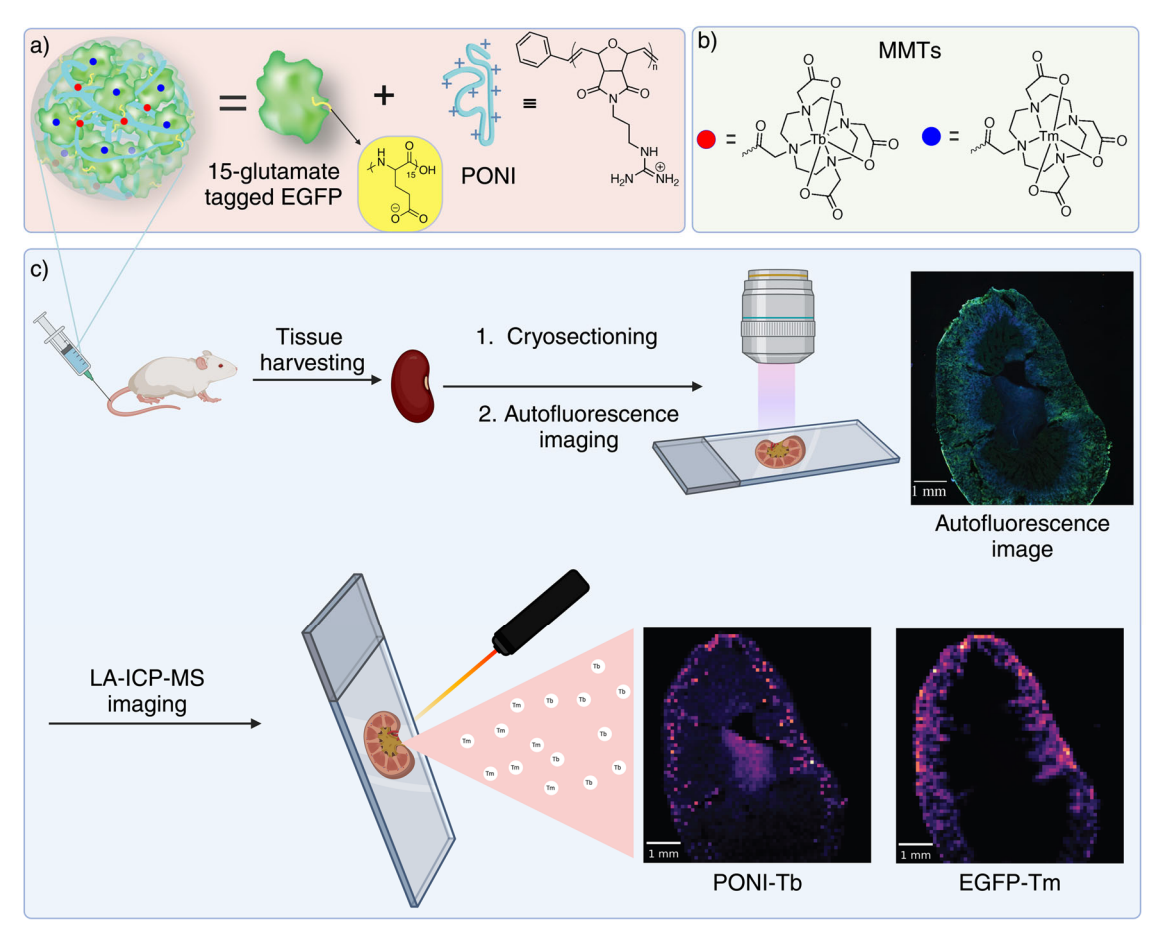


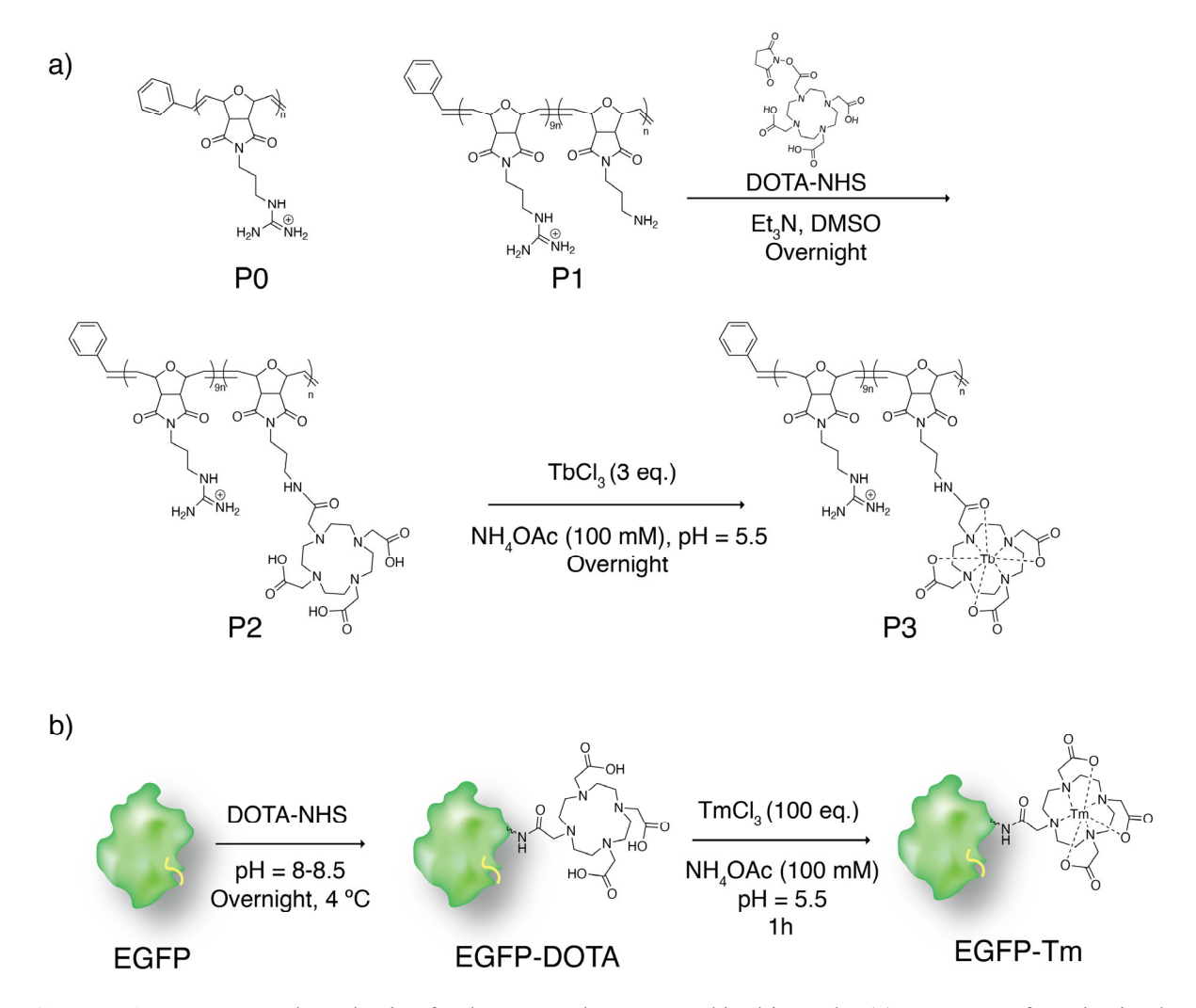
Figure 1. Metal-coded mass tags (MMTs) for sub-organ measurements of the quantitative tissue distributions of protein cargo and polymeric carrier. (a) Polymer-protein nanocomposites used in this work. Enhanced green fluorescent protein (EGFP) with a 15 glutamate-residue tag was used as the model protein cargo, and guanidinium-functionalized poly(oxanorborneneimide) (PONI) polymers were used as the delivery system. (b) Structures of the MMTs that were conjugated to EGFP and PONI. (c) Experimental workflow for quantitatively measuring the sub-organ biodistributions of MMT-PPNCs *in vivo*.

as they can form polymer-protein nanocomposites (PPNCs) capable of delivering proteins directly into the cytosol of cells.^{59–62} Using MMTs and LA-ICP-MS imaging, we quantified the site-specific tissue distribution of a model protein cargo. Using the inherent multiplexing capability of MS, we simultaneously quantified the protein and polymeric nanomaterial delivery system, providing quantitative information about the relative distributions of the carrier and cargo. This ability to image both vector and protein provides more insight into the relative fate of the delivery system and its protein cargo, affording quantitative correlations between nanocarrier structural properties and cargo biodistribution.

RESULTS AND DISCUSSION

MMTs Do Not Affect the Biophysical Characteristics of PPNCs

MMT-PPNCs were self-assembled using a homopolymer P0 (MW 55 kDa) with guanidinium groups and a diblock polymer P1 (structures shown in Scheme 1a) with guanidinium and amine groups in the ratio 9:1 (MW 64 kDa) (see Figures S1 & S2 for polymer characterization results). The polymers were synthesized using previously reported procedures.^{59,63} Next, a Tb-coded mass tag was loaded on P1 in two steps. First, DOTA was conjugated to P1 to yield P2. Then, Tb³⁺ was complexed to P2 to yield P3 (Scheme 1). After complexation, the excess-free Tb³⁺ was removed using Na₂EDTA, followed by centrifugal filtration. The number of filtration steps required to remove noncomplexed Tb³⁺ was determined by comparing the signal of Tb (Figure S3a) associated with P2 and P0 (used as a control). Two wash cycles were found to be sufficient to remove nonspecifically bound Tb³⁺. Similarly, a Tm-coded mass tag was loaded on EGFP (Scheme 1). Three wash cycles (Figure S3b) were needed to remove nonspecifically bound Tm³⁺



Scheme 1. Structure and synthesis of polymers and EGFP used in this study. (a) Structure of synthesized homopolymer P0, diblock copolymer P1, and synthesis route to conjugate Tb-coded mass tag on P1. (b) Tm-coded mass tag conjugation on EGFP. The yellow curved line is the polyglutamate (E-tag) that has 15 glutamate residues.

from the protein. LC-ESI-MS analysis indicated that 1.7 Tm on average were attached to each EGFP molecule (Figure S3c and d).

We next assessed the influence of the MMTs on the biophysical properties of the PPNCs. PPNCs were formulated by mixing varying proportions (0%, 5% and 100%) of P3 with P0 and EGFP-Tm (Figure S4a). Dynamic light scattering (DLS) measurements (in PBS, 150 mM NaCl, pH = 7.4) revealed that 5% P3 had no significant impact on the size (Figure S4b) or zeta potential

(Figure S4c) of the nanocomposites. Additionally, 5% P3 did not affect the in vitro protein delivery efficiency unlike 100% P3, which notably reduced efficiency (Figure S4d-f).

PPNCs were also subjected to shear force or heparin sulfate, which is a negatively charged competitor of EGFP-Tm, in 50% serum to evaluate their stability with conjugated MMTs. Native gel electrophoresis showed that 5% P3 did not compromise stability under shear force (Figure S4g). As a positive control, when exposed to heparin sulfate, some EGFP-Tm was displaced from the PPNCs with either 5% or 0% P3. Overall, these results indicate that 5% P3 does not affect PPNC properties or stability, allowing the MMTs to be used as a proxy of carriers and protein *in*

Table 1. ICP-MS analyses of Tb (i.e., PONI) and Tm (i.e., EGFP) in PPNCs treated mice (n=3) organs.

Organ	Tb (ppb)	Tm (ppb)	Tm / Tb
Injection sample ^a	11.90 ± 0.04	29 ± 1	2.4 ± 0.1
small intestine ^b	4 ± 2	6 ± 1	1.5 ± 0.8
large intestine ^b	4 ± 1	5 ± 1	1.3 ± 0.4
$lung^b$	44 ± 7	60 ± 20	1.4 ± 0.5
heart ^b	6 ± 1	9 ± 2	1.5 ± 0.4
kidney ^b	30 ± 10	430 ± 90	14 ± 6
spleen ^b	44 ± 4	70 ± 20	1.6 ± 0.5
liver ^b	60 ± 20	34 ± 7	0.6 ± 0.2
$blood^b$	6 ± 2	12 ± 2	2.0 ± 0.7

^aThe concentrations in injection sample represents Tb or Tm amount (ppb) present in injection sample volume (n=3).

^bThe concentrations were calculated by the Tb or Tm amount (nanograms) divided by organ weight (grams).

vivo. Notably, our previous work⁵⁸ and other literature reports^{64–66} confirm the high stability of lanthanide DOTA chelates in various conditions, including human serum, so no metal loss is expected *in vivo*.

LA-ICP-MSI Provides a Reliable In Situ Measure of PPNC Components

After demonstrating that PPNCs with 5% P3 are stable and retain their physical and biological properties in simulated *in vivo* conditions, PPNCs (0.67 mg/mL of PONI, 8 μM of EGFP; total guanidinium (G) and glutamate (E) ratio or G/E = 20) with 5% P3 and EGFP-DOTA-Tm were intravenously injected into mice. After 0.5 h, the mice were sacrificed, and organs were harvested, homogenized, and analyzed by ICP-MS (Table 1). As previously reported with analogous PPNCs,⁴¹ a significant amount of the tagged EGFP and PONI polymer accumulated in the lungs, highlighting the potential of this delivery system to target and treat lung diseases. Interestingly, EGFP and the PONI polymer appear to have different excretion pathways as

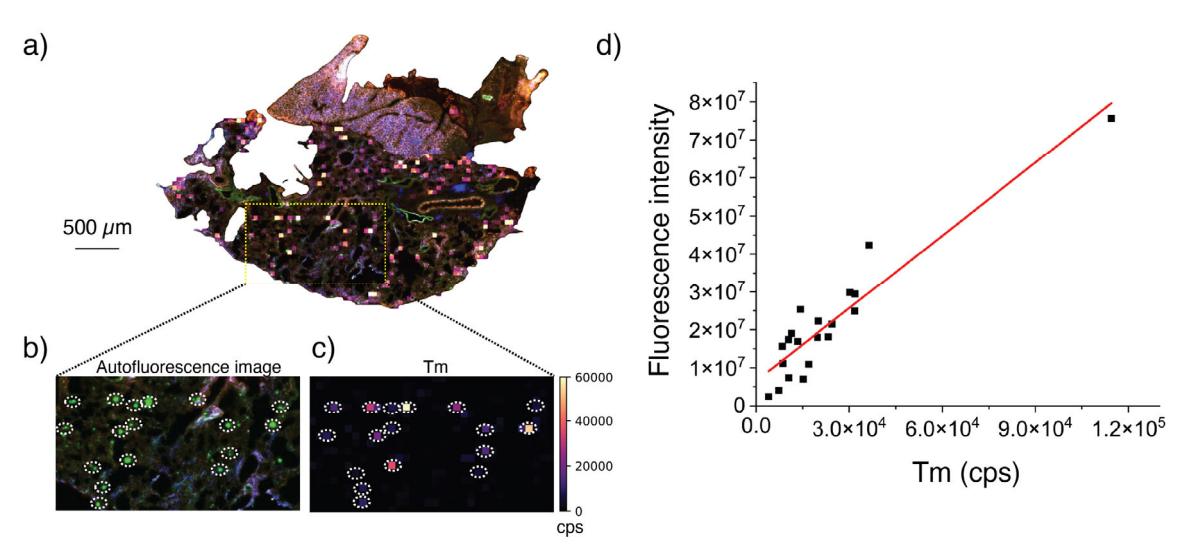


Figure 2. LA-ICP-MSI provides reliable information about the biodistribution of PPNC's components. (a) Overlay of fluorescence and Tm ion image of lung tissue from mice injected with MMT-PPNCs. (b) and (c) are zoomed-in regions from Figure 2a, indicating excellent spatial correlation between fluorescence signals of EGFP and Tm ion signals of EGFP. (d) Correlation between the fluorescence intensity of EGFP and Tm ion intensity in 20 randomly selected spots, indicating a strong correlation between EGFP's fluorescent signal and Tm ion signal.

indicated by their different amounts in the kidney and liver. Based on the results in the lung, kidney, and liver, these organs were chosen for quantitative imaging.

We first compared the spatial distributions of EGFP in the lung as measured by its green fluorescence to the distribution of Tm signals from LA-ICP-MS imaging of the same tissue section. As shown in Figures 2a-c (and Figures S5a, c), we find excellent spatial correlations between the green fluorescence and Tm signal in the LA-ICP-MS, indicating that the metal is not lost *in vivo* and that LA-ICP-MS imaging provides a reliable measure of the metal-tagged components. Moreover, a comparison of the fluorescence and Tm signal levels from 20 randomly selected locations (Figures 2d and S5b, d) reveal a strong correlation.

Simultaneous LA-ICP-MS Imaging of Polymeric Carrier and its Protein Cargo

Because both EGFP and the PONI polymer are labeled with distinct MMTs, LA-ICP-MSI enables the simultaneous imaging of the bio-distributions of both the cargo and carrier, offering insights into their co-localization. EGFP (Figure 3a) and the PONI polymer (Figure 3b) are broadly distributed in the lung (Figure 3). An overlaid image of their distributions (Figure 3c) reveals that the protein and polymer are largely, but not perfectly, co-localized with a Pearson's correlation coefficient of 0.8. Comparing the LA-ICP-MS images with an optical image (Figure 3d-j) enables a determination of the specific sub-organ regions where the polymer and protein are located. From this comparison, we find that both the EGFP and PONI polymer are primarily distributed in the alveolar region (Figure 3a, b). The materials are generally not found in the conducting or respiratory airways (Figure 3h-j). Moreover, there is no PONI polymer or EGFP in connective tissue, but there are detectable amounts of the PONI polymer in the pulmonary blood vessels, while no signal for EGFP is found there (Figures 3e-g). The LA-ICP-MSI measurements here provide

better site-specific information about the sub-organ regions where the polymer and protein localize in the lungs. Such site-specific information about how the components of delivery systems are distributed in the lung could be further utilized to optimize therapeutic delivery in the lung.

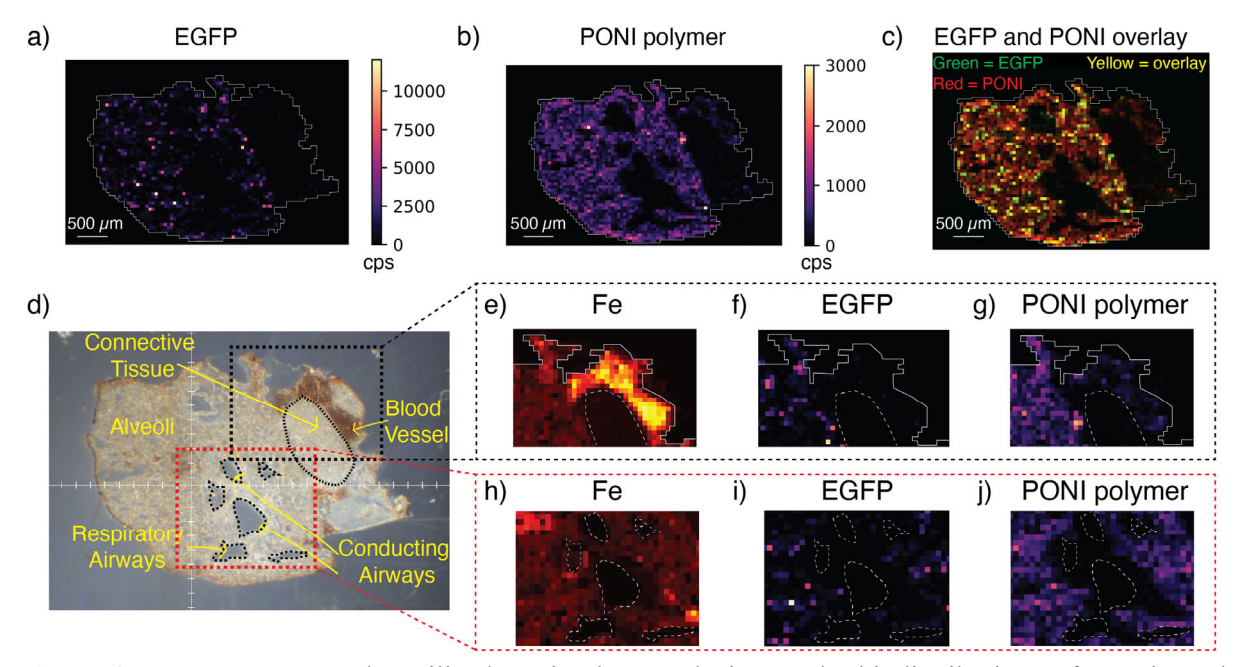


Figure 3. LA-ICP-MSI can be utilized to simultaneously image the biodistributions of protein and carrier in lung section of mice injected with PPNCs. (a) Tm image from LA-ICP-MSI, indicating distribution of EGFP. (b) Tb image from LA-ICP-MSI, indicating the distribution of the PONI polymer. (c) Overlay of the Tm and Tb signal, indicating the co-localization of EGFP and PONI. PONI is shown in red and EGFP is shown in green. The yellow color represents the region where both EGFP and PONI are co-localized. (d) Optical image of the lung tissue section prior to LA-ICP-MSI analysis. (e) Fe image from LA-ICP-MSI of the region highlighted by the black box in 3d. The high Fe signal shows the location of pulmonary blood vessel, whereas very low Fe signals indicate the connective tissue. (f) EGFP distribution from the Tm signal in the region highlighted by the black box in 3d. (h) Fe image from LA-ICP-MSI of the region highlighted by the red box in 3d. The absence of Fe in the encircled regions indicates respiratory and conducting airways. (i) EGFP distribution from the Tm signal in the region highlighted by the red box in 3d. (j) PONI polymer distribution from the Tm signal in the region highlighted by the red box in 3d.

Sub-organ Level Quantitative Imaging of Polymeric Carrier and Protein Cargo

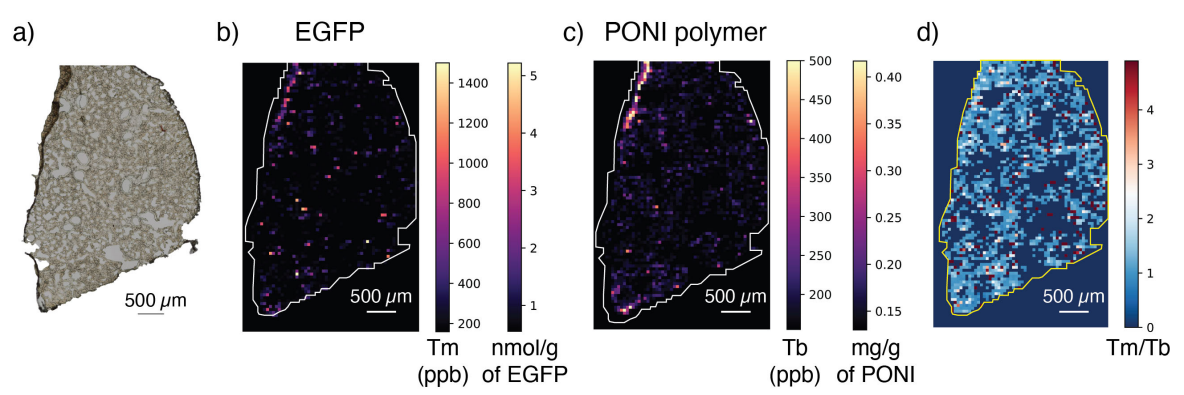


Figure 4. LA-ICP-MSI can determine site-specific concentrations of protein cargo and its carrier. (a) Optical image of the lung tissue from a mouse injected with PPNCs. (b) Tm (ppb) and corresponding EGFP concentration (nmol/g) distributions in the lung. See the Supporting Information for the calculation that converts Tm concentration to EGFP concentration. (c) Tb (ppb) and corresponding PONI polymer concentration (mg/g) distributions. See the Supporting Information for the calculation that converts Tb concentration to mg/g of PONI polymer. (d) Image showing the ratios of EGFP (Tm) to PONI polymer (Tb). White pixels represent a Tm/Tb ratio of 2.4, which was the injected ratio. Dark blue pixels corresponding to Tm/Tb ratio of 0 represents places where EGFP and/or PONI polymers were below the limit of quantification (LOQ).

Site-specific concentrations of the delivery system components were further determined in the lung using our recently developed quantitative imaging approach (see Supporting Information for details).⁶⁷ By applying an imaging calibration (Figure S6), the concentrations of the protein and polymer at any given location can be obtained (Figure 4). Considering that there are ~ 1.7 Tm per EGFP molecule (Figure S3d), we can calculate the moles of EGFP that are delivered to the different regions of the lung (Figure 4b and Figure S7). The heterogeneous distribution of the EGFP (i.e., Tm ppb) (Figure 4b) emphasizes the value of determining local concentrations. Clearly, the protein cargo is not distributed equally throughout the alveolar regions but rather is concentrated in certain regions. Considering all the pixels from three separate lung tissue sections, we find local protein amounts as low as 5 and as high as 290 attomoles, which correspond to concentrations from 0.3 to 19.6 nmol/g, but most pixels with detectable protein have a concentration around 0.6 ± 0.1 nmol/g (Figure S8). Studies have shown that 0.03 nmol/g to 3 nmol/g concentrations of antibodies can have a therapeutic effect when present in tissues, 68,69 suggesting that the amount of protein delivered by the PPNCs in our experiments provides dosing

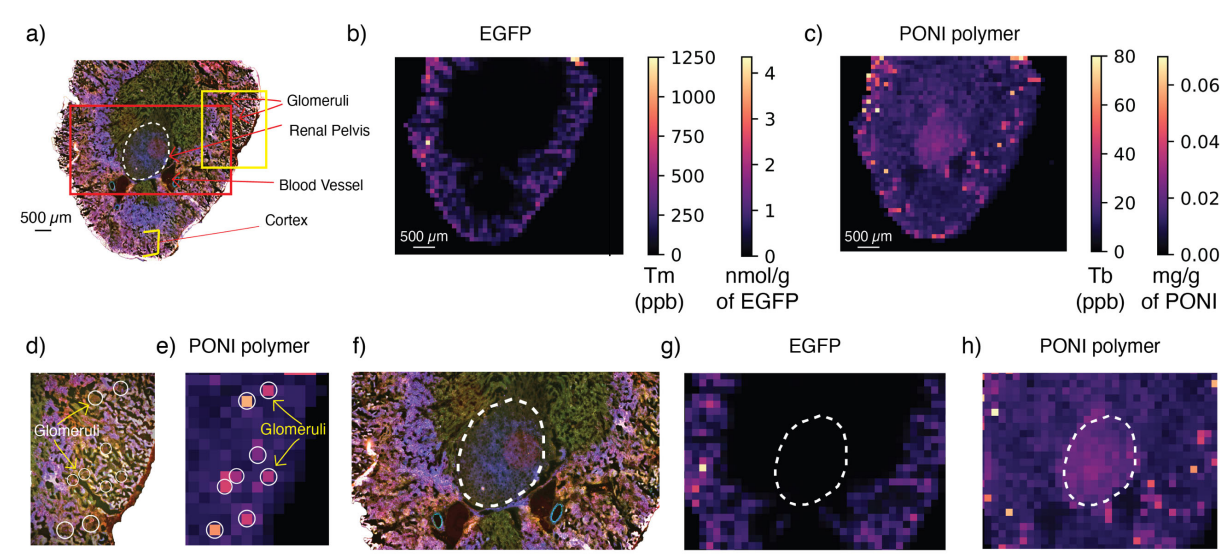


Figure 5. EGFP and the PONI polymer have distinct quantitative distributions in the kidney, indicating different renal excretion behavior. (a) Autofluorescence image of a kidney section from a mouse injected with PPNCs, highlighting the different sub-organ regions in the kidney. (b) Tm (ppb) and corresponding EGFP concentrations (attomoles) in the kidney, showing that EGFP is primarily present in the cortex region of the kidney. (c) Tb (ppb) and corresponding PONI polymer concentrations in the kidney, showing that PONI is more broadly distributed in the kidney. (d) Expanded region of the autofluorescence image within the highlighted solid yellow box from 5a. (e) Expanded region showing the Tb and corresponding PONI polymer distribution within the highlighted solid yellow box from 5a. High levels of Tb in the glomeruli (circled in white) indicate that the PONI polymer is relatively enriched in the glomeruli. (f) Expanded region of the fluorescence image within the highlighted red box from 5a. The renal pelvis is circled by a white dashed line. (g) Expanded region showing the Tm and corresponding EGFP distributions within the highlighted red box from 5a. Measured Tb in the renal pelvis indicates that the PONI polymer is being excreted via urine, whereas EGFP is not.

in a meaningful window. Likewise, the quantitative spatial distributions of the PONI polymer can also be determined from the Tb signals (Figure 4c). The polymer concentrations range from 0.1 to 1.0 mg/g. The relative quantitative distributions of Tm and Tb provide additional insight into the release of EGFP from the PPNCs. Locations in the lung with Tm/Tb ratios greater than the injected ratio of 2.4 (white in Figure 4d) likely indicate the presence of free (or released) EGFP. Considering the images of the lung sections in Figures 4 and S7, 15% of the pixels with quantifiable protein have ratios above 2.4, indicating these regions have released protein. Of course, this percentage should be considered a lower limit of sites with free protein, as pixels with values less than 2.4 could also have released protein.

Kidney sections were also imaged by LA-ICP-MS to track renal excretion of the PPNCs. From measurements of tissue homogenates (Table 1), we find that protein levels in the kidney are significantly higher than polymer levels. However, LA-ICP-MSI reveals that EGFP (Figure 5b) and the polymer (Figure 5c) have different distributions (Pearson correlation = 0.5) in the kidney, with EGFP primarily distributed in the cortex region and the PONI polymer more heterogeneously distributed. Polymer and protein levels were quantified in the glomeruli, renal pelvis, and blood vessels (Table 2). The glomeruli and renal pelvis can be readily identified by comparison with autofluorescence images (e.g., Figures 5d & 5f). The blood vessels can be located either optically or by measuring the Fe signals in LA-ICP-MS images (e.g., Figure S9). The polymer is relatively enriched in the glomeruli (Figure 5e) and renal pelvis (Figure 5h) with average concentrations of 0.04 ± 0.02 mg/g and 0.03 ± 0.01 mg/g, respectively. While EGFP is more abundant than the polymer in the cortex and has an average concentration of 1.3 ± 0.5 nmol/g in the glomeruli, there is no quantifiable EGFP in the renal pelvis (Figure 5g). These results indicate that the polymer is being excreted more rapidly through the kidney than EGFP, which is an important insight because it can be difficult to predict the renal clearance for a given nanomaterial as it depends on multiple factors such as its size, 70 charge, 71 and shape. 72

A comparison of the EGFP and polymer levels in the kidney cortex provide further insight into PPNC excretion. The Tm:Tb (protein:polymer) ratios in the cortex are generally higher than the Tm:Tb ratio in the injected sample (Figure S10), indicating that the PPNCs are disassembled when present in the kidney cortex. This disassembly behavior aligns with previous kidney distribution findings for polymer/siRNA delivery systems.⁷³ Moreover, anionic polymers based on oligo(ethylene glycol) methyl ether methacrylate have been shown to selectively accumulate in the cortex of the kidney,⁷⁴ analogous to our observations with negatively-charged EGFP in our

experiments here. Interestingly, there is no quantifiable polymer or EGFP in blood vessels (Table 2), which is consistent with the low levels of the PONI polymer and protein measured in the blood after 0.5 h (Table 1).

A comparison of PONI polymer and EGFP distributions in the liver (Figure 6) indicates that the PONI polymer is more broadly distributed than EGFP, but the polymer has a narrower range of concentrations. Polymer levels vary from 0.018 mg/g, which is the limit of quantitation, up to 0.087 mg/g. The amounts of EGFP vary from 0.03 to 0.15 nmol/g. These protein concentrations are much lower than the protein concentrations found in the alveoli of the lung or the cortex of the kidney. The punctate distribution of EGFP (Figure 6b), along with a Pearson correlation of 0.6, suggests that PONI and EGFP are not co-localized as well in the liver as they are in the lung. Upon comparing autofluorescence and LA-ICP-MS images of the liver (Figures 6d-g), we find that both the PONI polymer and EGFP are found primarily in the liver parenchyma and are not present in the blood vessels or portal triads. These distributions suggest that the PPNCs

Table 2. Quantitative analysis of LA-ICP-MS images (n=3) of PONI polymer and EGFP in different sub-organs of the kidney.

Sub-organ of Kidney	PONI polymer (mg/g) ^a	EGFP (nmol/g) ^b
Glomeruli ^c	0.04 ± 0.02	1.3 ± 0.5
Renal Pelvis ^d	0.03 ± 0.01	e
Blood Vesself	g	e

^aThe PONI polymer concentrations were determined from average Tb (ppb) concentration (see Supporting Information for more details) contained in all pixels corresponding to glomeruli, renal pelvis, and blood vessels.

^gBelow the LOQ of Tb which was 25 ppb as determined from 10 times the signal of background.

are rapidly taken up in surrounding tissue and are cleared from circulation. Some reports have suggested that polymeric delivery systems that rely on electrostatic assembly, like the PPNCs in our work, can dissociate and distribute differently in the liver due to the presence of collagen and heparin sulfate in the extracellular matrix of hepatic sinusoids. Positively-charged carrier materials are readily taken up into hepatocytes, while negatively-charged cargo tend to distribute into Kupffer cells. The distinct distributions of the PONI polymer and EGFP in the kidney and liver indicate that the carrier and cargo are being excreted via different mechanisms, underscoring the effectiveness of our method in providing more insight on the excretion dynamics of delivery systems.

^bThe EGFP concentrations were determined from average Tm (ppb) concentration (see Supporting Information for more details) contained in pixels corresponding to glomeruli, renal pelvis, and blood vessels

^cPixels associated with glomeruli were found manually by comparing glomeruli identified in autofluorescence images (e.g. Figure 5a) with the corresponding locations in the LA-ICP-MS images (e.g. Figure 5b and c).

^dPixels associated with renal pelvis were found by comparing autofluorescence images (e.g. Figure 5a) and LA-ICP-MS images (e.g. Figure 5b and c).

^eBelow the LOQ of Tm, which was 70 ppb as determined from 10 times the signal of background.

^fPixels associated with blood vessels were found by comparing optical images and LA-ICP-MS images of Fe, as shown in Figure S9.

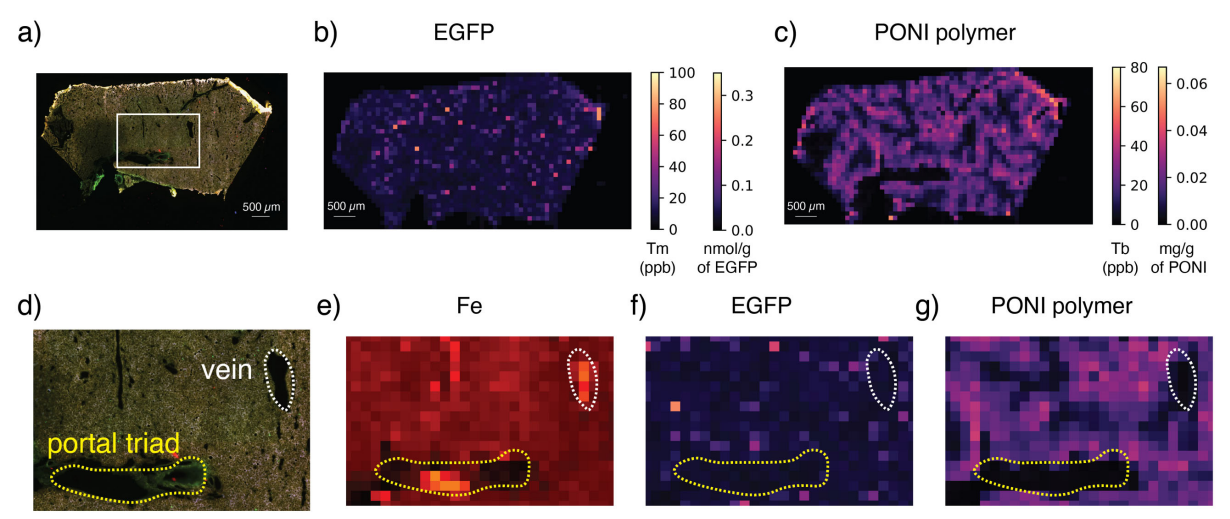


Figure 6. EGFP and the PONI polymer have distinct quantitative distributions in the liver, indicating different excretion behavior. (a) Autofluorescence image of a liver section from a mouse injected with PPNCs. (b) Tm (ppb) and corresponding EGFP concentrations in the liver, showing a punctate distribution of protein. (c) Tb and corresponding PONI polymer concentration in the liver, showing a broad distribution of the polymer in the liver parenchyma. (d) Expanded region of the autofluorescence image within the highlighted white box from 6a. The vein is circled by a dashed white line, and the portal triad is circled by a dashed yellow line. (e) Fe image from LA-ICP-MSI of the region highlighted by the white box in 6a. The relatively high Fe signal shows the location of vein. (f) Expanded region showing the Tm and corresponding EGFP distribution within the highlighted white box from 6a. The absence of Tm in the vein (shown by dashed white line) and the portal triad (shown by dashed yellow line) indicates that EGFP is only present in liver parenchyma. (g) Expanded region showing the Tb and corresponding PONI polymer distributions within the highlighted white box from 6a. The absence of Tb in the vein (shown by dashed white line) and the portal triad (shown by dashed yellow line) indicates that PONI polymer is only present in liver parenchyma.

CONCLUSIONS

We have developed an imaging method that can determine the absolute site-specific concentrations of proteins and their nanocarriers in tissues. This method utilizes thermodynamically stable and kinetically inert DOTA-lanthanide chelates as mass tags that reliably report the spatial distributions of both cargo and carrier. Site-specific quantitation of the protein cargo and its carrier are possible via the use of quantitative LA-ICP-MS imaging. Application of this method demonstrates that PONI polymer carriers deliver protein to the alveolar region of the lung at therapeutically relevant doses, confirming the potential of these delivery systems for treating lung disease. Moreover, using the multiplexing capability of LA-ICP-MS imaging, we find that the polymer carrier and protein are mostly co-localized in the lungs, but they

are not co-localized in the kidney and liver, indicating they have different excretion pathways. Looking forward, we expect that our quantitative imaging approach will be able to provide critically important pharmacokinetic and pharmacodynamic data for protein therapeutics, while at the same time yielding sub-organ information that will help evaluate tissue penetration and possible off-target effects.

EXPERIMENTAL SECTION

Further details about the chemicals and materials used in this work, and the experiments conducted to evaluate the effect of MMTs on PPNC's size, charge, stability, and cellular delivery can be found in the Supporting Information.

Formulation of MMT – conjugated PPNCs. Using previously reported procedures^{59,63} homopolymer P0 (MW 55 kDa) with guanidinium groups and diblock polymer P1 with guanidinium and amine groups (MW 64 kDa) were synthesized by ring-opening metathesis polymerization (Scheme 1; Figures S1 & S2). Next, the P1 polymer was conjugated with dodecane tetraacetic acid (DOTA) in dry dimethylsulfoxide (DMSO) to synthesize DOTA-conjugated polymer P2 (Figure S1). The resultant reaction mixture was dialyzed (Thermo Scientific™ SnakeSkin™ Dialysis Tubing, MWCO = 10 kDa) in water for 24 h. Then, as described in our previous work,⁵⁸ the purified P2 polymer was complexed with Tb³⁺, ultracentrifuged to get rid of free Tb³⁺, and lyophilized to obtain the Tb-tagged polymer P3. The success of Tb³⁺ complexation was characterized by ICP-MS.

Enhanced green fluorescent protein (EGFP) with a 15-residue glutamate tag at the C-terminus was expressed as previously reported.^{78,79} Next, EGFP was conjugated with DOTA in a

sodium bicarbonate buffer (100 mM, pH 8-8.5) and stirred overnight at 4 °C (Scheme 1). Then, Tm³+ was complexed to EGFP-DOTA using the same procedure as used for polymers. Purified EGFP-DOTA-Tm was then buffer exchanged with Dulbecco's Phosphate Buffered Saline (DPBS) and stored at 4 °C until used for the PPNC formulations. High-performance liquid chromatography coupled with electrospray ionization HPLC-ESI-MS was used to determine the extent of Tm complexation to EGFP.

PPNCs were generated by a "mix and wait" strategy as described previously.⁵⁹ Briefly, polymer and protein were mixed making sure that the charge ratio (total guanidinium and glutamate ratio or G/E ratio) was 20. To create metal-tagged PPNCs, control polymer P0 was mixed with a given percentage of P3, and then EGFP-DOTA-Tm was added to the resultant mixture. After adding EGFP-DOTA-Tm, the mixture was left at room temperature for 10 minutes, and then the sample was diluted with DPBS or DPBS followed by cell culture media as needed to perform *in vivo* and *in vitro* experiments respectively.

Evaluation of the effect of MMTs on PPNCs. The experimental details associated with the measurements of size, surface charge, stability, and *in vitro* uptake of PPNC with or without P3 can be found in the Supporting Information.

Intravenous administration of PPNCs *in vivo*. Details about the animal experiments and associated animal welfare protocols are provided in the Supporting Information.

Microscopy Imaging. Prior to LA-ICP-MSI, tissue sections from treated mice were imaged by a Keyence BZ-X800 microscope. All tissue sections were imaged by brightfield optical microscopy and by autofluorescence in red, green, and blue channels. Tissue sections were imaged using either 10x (for kidney and liver) or 20x (for lung) objective lenses. An overlay image of red, green, and blue channels was constructed using a BZ-X800 analyzer. Adobe Photoshop was used whenever

necessary for removing the background and adjusting the contrast of images. Optical images of all tissues were also acquired from a camera mounted in the laser ablation system. Fluorescence signal intensities of EGFP clusters were quantified using NIS element software (Nikon).

LA-ICP-MS imaging and analysis. Tissue sections for LA-ICP-MSI were prepared as discussed in Supporting Information. LA-ICP-MSI experiments were conducted on a PerkinElmer NEXION 300X ICP-MS using a Teledyne CETAC LSX-213 G2 laser ablation system attached to the ICP-MS via Teflon tubing. Tissues were ablated using the line scanning mode, whereby the laser spot size was either 50 µm (for lung sections) or 100 µm (for liver and kidney sections). The laser energy employed was 3.34 J/cm² with 70% laser power. All tissue samples were measured for isotopes of ⁵⁷Fe, ¹⁵⁹Tb (proxy of PONI), ¹⁶⁹Tm (proxy of EGFP), and ¹⁶⁵Ho (standard for normalization). The instrument was operated under the following conditions: He gas flow = 0.8L/min; laser scan rate = $20 \mu m/s$; laser frequency = 10 Hz, and shutter delay = 10 s. All the LA-ICP-MS raw data was reconstructed into images, segmented, analyzed, and quantified using the Python script RecSegImage-LA⁸⁰ which is freely available at GitHub (https://github.com/Vachet-Lab/RecSegImage-LA). This Python script was also used to calculate the Pearson correlation coefficients for the biodistribution of EGFP and PONI. Signal intensities corresponding to the determined limit of detection from calibration curves were used as the thresholds for correlation coefficient calculations.

ACKNOWLEDGEMENT

Parts of the images in the table of contents figure and Figure 1 were created with BioRender.com. R.W.V. and V.M.R. acknowledge support from the National Science Foundation under grant CHE-2108044. V.M.R. acknowledges support from National Institutes of Health DK121351 and EB022641. The authors also acknowledge the use of the UMass Amherst Mass Spectrometry Core

Facility for some of the measurements (RRID:SCR_019063). The microscopy data was gathered in the Light Microscopy Facility and Nikon Center of Excellence at the Institute for Applied Life Sciences, UMass Amherst with support from the Massachusetts Life Sciences Center (RRID:SCR_021148).

AUTHOR CONTRIBUTIONS

D.K.A., V.M.R. and R.W.V. conceived the idea, designed the experiments, and wrote the manuscript; D.K.A. performed the MMTs conjugation, characterization, tissue cryosectioning, *in vivo* whole organ quantification, tissue autofluorescence and LA-ICP-MS imaging experiments. Teerapong J. fabricated the gelatin-containing quantitative imaging platform and wrote the python scripts for analyzing the imaging data. R.G. and Y.A.C. synthesized the polymers and protein; R.G. and Y.A.C. characterized the PPNCs. R.G., Y.A.C., Taewon J. performed the animal experiments. K.T. assisted in MMTs conjugation to the proteins and *in vivo* quantification experiments. J.B. characterized the protein by ESI-MS. All authors edited the manuscript.

SUPPORTING INFORMATION

Additional information, including the synthetic materials and methods, characterization methods and results from LC-ESI-MS, flow cytometry, ICP-MS, and gel electrophoresis, administration of the PPNCs *in vivo*, and calculations of protein and polymer concentrations can be found in the Supporting Information section. The Supporting Information is available free of charge on the ACS Publications website at DOI:

REFERENCES

(1) Martin, K. P.; Grimaldi, C.; Grempler, R.; Hansel, S.; Kumar, S. Trends in Industrialization of Biotherapeutics: A Survey of Product Characteristics of 89 Antibody-Based Biotherapeutics. *MAbs* **2023**, *15* (1), 1–29.

- (2) Chen, Z.; Wang, X.; Chen, X.; Huang, J.; Wang, C.; Wang, J.; Wang, Z. Accelerating Therapeutic Protein Design with Computational Approaches toward the Clinical Stage. *Comput Struct Biotechnol J* **2023**, *21*, 2909–2926.
- (3) Wu, J.; Sahoo, J. K.; Li, Y.; Xu, Q.; Kaplan, D. L. Challenges in Delivering Therapeutic Peptides and Proteins: A Silk-Based Solution. *Journal of Controlled Release* **2022**, *345* (February), 176–189.
- (4) Jiskoot, W.; Randolph, T. W.; Volkin, D. B.; Middaugh, C. R.; Schöneich, C.; Winter, G.; Friess, W.; Crommelin, D. J. A.; Carpenter, J. F. Protein Instability and Immunogenicity: Roadblocks to Clinical Application of Injectable Protein Delivery Systems for Sustained Release. *J Pharm Sci* **2012**, *101* (3), 946–954.
- (5) Kinderman, F.; Yerby, B.; Jawa, V.; Joubert, M. K.; Joh, N. H.; Malella, J.; Herskovitz, J.; Xie, J.; Ferbas, J.; McBride, H. J. Impact of Precipitation of Antibody Therapeutics After Subcutaneous Injection on Pharmacokinetics and Immunogenicity. *J Pharm Sci* 2019, 108 (6), 1953–1963.
- (6) Schuster, J.; Koulov, A.; Mahler, H. C.; Detampel, P.; Huwyler, J.; Singh, S.; Mathaes, R. In Vivo Stability of Therapeutic Proteins. *Pharm Res* **2020**, *37* (2).
- (7) Zaman, R.; Islam, R. A.; Ibnat, N.; Othman, I.; Zaini, A.; Lee, C. Y.; Chowdhury, E. H. Current Strategies in Extending Half-Lives of Therapeutic Proteins. *Journal of Controlled Release* **2019**, *301* (March), 176–189.
- (8) Baker, M. P.; Reynolds, H. M.; Lumicisi, B.; Bryson, C. J. Immunogenicity of Protein Therapeutics: The Key Causes, Consequences and Challenges. *Self/Nonself Immune Recognition and Signaling* **2010**, *I* (4), 314–322.
- (9) Yanover, C.; Jain, N.; Pierce, G.; Howard, T. E.; Sauna, Z. E. Pharmacogenetics and the Immunogenicity of Protein Therapeutics. *Nat Biotechnol* **2011**, *29* (10), 870–873.
- (10) Jawa, V.; Cousens, L. P.; Awwad, M.; Wakshull, E.; Kropshofer, H.; De Groot, A. S. T-Cell Dependent Immunogenicity of Protein Therapeutics: Preclinical Assessment and Mitigation. *Clinical Immunology* **2013**, *149* (3 PB), 534–555.
- (11) Dembélé, J.; Liao, J. H.; Liu, T. P.; Chen, Y. P. Overcoming Cytosolic Delivery Barriers of Proteins Using Denatured Protein-Conjugated Mesoporous Silica Nanoparticles. *ACS Appl Mater Interfaces* **2023**, *15* (1), 432–451.
- (12) Scaletti, F.; Hardie, J.; Lee, Y. W.; Luther, D. C.; Ray, M.; Rotello, V. M. Protein Delivery into Cells Using Inorganic Nanoparticle-Protein Supramolecular Assemblies. *Chem Soc Rev* **2018**, *47* (10), 3421–3432.
- (13) Mitchell, M. J.; Billingsley, M. M.; Haley, R. M.; Wechsler, M. E.; Peppas, N. A.; Langer, R. Engineering Precision Nanoparticles for Drug Delivery. *Nat Rev Drug Discov* 2021, 20 (2), 101–124.
- (14) Pudlarz, A.; Szemraj, J. Nanoparticles as Carriers of Proteins, Peptides and Other Therapeutic Molecules. *Open Life Sci* **2018**, *13* (1), 285–298.
- (15) Solaro, R.; Chiellini, F.; Battisti, A. *Targeted Delivery of Protein Drugs by Nanocarriers*; 2010; Vol. 3.

- (16) Ait-Belkacem, R.; Berenguer, C.; Villard, C.; Ouafik, L.; Figarella-Branger, D.; Beck, A.; Chinot, O.; Lafitte, D. Monitoring Therapeutic Monoclonal Antibodies in Brain Tumor. *MAbs* **2014**, *6* (6), 1385–1393.
- (17) Spruill, M. L.; Maletic-Savatic, M.; Martin, H.; Li, F.; Liu, X. Spatial Analysis of Drug Absorption, Distribution, Metabolism, and Toxicology Using Mass Spectrometry Imaging. *Biochem Pharmacol* **2022**, *201* (May), 115080.
- (18) Joshi, V. B.; Geary, S. M.; Salem, A. K. Biodegradable Particles as Vaccine Delivery Systems: Size Matters. *AAPS Journal* **2013**, *15* (1), 85–94.
- (19) Doddapaneni, B. S.; Kyryachenko, S.; Chagani, S. E.; Alany, R. G.; Rao, D. A.; Indra, A. K.; Alani, A. W. G. A Three-Drug Nanoscale Drug Delivery System Designed for Preferential Lymphatic Uptake for the Treatment of Metastatic Melanoma. *Journal of Controlled Release* **2015**, *220*, 503–514.
- (20) Tseng, Y. C.; Xu, Z.; Guley, K.; Yuan, H.; Huang, L. Lipid-Calcium Phosphate Nanoparticles for Delivery to the Lymphatic System and SPECT/CT Imaging of Lymph Node Metastases. *Biomaterials* **2014**, *35* (16), 4688–4698.
- (21) Toy, R.; Peiris, P. M.; Ghaghada, K. B.; Karathanasis, E. Shaping Cancer Nanomedicine: The Effect of Particle Shape on the in Vivo Journey of Nanoparticles. *Nanomedicine*. Future Medicine Ltd. 2014, pp 121–134.
- (22) Xiao, Q.; Zoulikha, M.; Qiu, M.; Teng, C.; Lin, C.; Li, X.; Sallam, M. A.; Xu, Q.; He, W. The Effects of Protein Corona on in Vivo Fate of Nanocarriers. *Adv Drug Deliv Rev* **2022**, *186*, 114356.
- (23) Poon, W.; Zhang, Y. N.; Ouyang, B.; Kingston, B. R.; Wu, J. L. Y.; Wilhelm, S.; Chan, W. C. W. Elimination Pathways of Nanoparticles. *ACS Nano* **2019**, *13* (5), 5785–5798.
- (24) Du, B.; Yu, M.; Zheng, J. Transport and Interactions of Nanoparticles in the Kidneys. *Nat Rev Mater* **2018**, *3* (10), 358–374.
- (25) Williams, S. P. Tissue Distribution Studies of Protein Therapeutics Using Molecular Probes: Molecular Imaging. *AAPS Journal* **2012**, *14* (3), 389–399.
- (26) Vasquez, K. O.; Casavant, C.; Peterson, J. D. Quantitative Whole Body Biodistribution of Fluorescent-Labeled Agents by Non-Invasive Tomographic Imaging. *PLoS One* **2011**, *6* (6).
- (27) Nessler, I.; Cilliers, C.; Thurber, G. M. Practical Guide for Quantification of in Vivo Degradation Rates for Therapeutic Proteins with Single-cell Resolution Using Fluorescence Ratio Imaging. *Pharmaceutics* **2020**, *12* (2).
- (28) Giddabasappa, A.; Gupta, V. R.; Norberg, R.; Gupta, P.; Spilker, M. E.; Wentland, J.; Rago, B.; Eswaraka, J.; Leal, M.; Sapra, P. Biodistribution and Targeting of Anti-5t4 Antibody-Drug Conjugate Using Fluorescence Molecular Tomography. *Mol Cancer Ther* 2016, 15 (10), 2530–2540.
- (29) Gupta, P.; Wentland, J. A.; Leal, M.; Ma, D.; Roach, R.; Esparza, A.; King, L.; Spilker, M. E.; Bagi, C.; Winkelmann, C. T.; Giddabasappa, A. Assessment of Near-Infrared Fluorophores to Study the Biodistribution and Tumor Targeting of an IL13 Receptor A2 Antibody by Fluorescence Molecular Tomography. *Oncotarget* **2017**, *8* (34), 57231–57245.

- (30) Wischhusen, J. C.; Wilson, K. E. In Vivo Immunofluorescence Localization for Assessment of Therapeutic and Diagnostic Antibody Biodistribution in Cancer Research. *Journal of Visualized Experiments* **2019**, *2019* (151), 1–8.
- (31) Vila-Caballer, M.; Codolo, G.; Munari, F.; Malfanti, A.; Fassan, M.; Rugge, M.; Balasso, A.; de Bernard, M.; Salmaso, S. A PH-Sensitive Stearoyl-PEG-Poly(Methacryloyl Sulfadimethoxine)-Decorated Liposome System for Protein Delivery: An Application for Bladder Cancer Treatment. *Journal of Controlled Release* **2016**, *238*, 31–42.
- (32) Grudén, S.; Brunmark, C.; Holmqvist, B.; Brenndörfer, E. D.; Johansson, M.; Liu, J.; Zhao, Y.; Axén, N.; Hassan, M. Biodistribution of Fluorescence-Labelled EGF Protein from Slow Release NanoZolid Depots in Mouse. *Int J Pharm* **2021**, *601* (April).
- (33) Wang, D.; Wang, T.; Yu, H.; Feng, B.; Zhou, L.; Zhou, F.; Hou, B.; Zhang, H.; Luo, M.; Li, Y. Engineering Nanoparticles to Locally Activate T Cells in the Tumor Microenvironment. *Sci Immunol* **2019**, *4* (37), 1–14.
- (34) Yan, Y.; Zhou, L.; Sun, Z.; Song, D.; Cheng, Y. Targeted and Intracellular Delivery of Protein Therapeutics by a Boronated Polymer for the Treatment of Bone Tumors. *Bioact Mater* **2022**, 7 (May 2021), 333–340.
- (35) Garousi, J.; Orlova, A.; Frejd, F. Y.; Tolmachev, V. Imaging Using Radiolabelled Targeted Proteins: Radioimmunodetection and Beyond. *EJNMMI Radiopharm Chem* **2020**, *5* (1).
- (36) Akanji, A. G.; Muramoto, E.; Filho, J. de S. C.; Couto, R. M.; de Araújo, E. B. Radiolabeling and Biodistribution of Monoclonal Antibody (MAb) Anti-CD20 with Iodine-131. *Brazilian Archives of Biology and Technology* **2005**, *48* (SPECIL ISS. 2), 69–72.
- (37) England, C. G.; Ehlerding, E. B.; Hernandez, R.; Rekoske, B. T.; Graves, S. A.; Sun, H.; Liu, G.; McNeel, D. G.; Barnhart, T. E.; Cai, W. Preclinical Pharmacokinetics and Biodistribution Studies of 89Zr-Labeled Pembrolizumab. *Journal of Nuclear Medicine* 2017, 58 (1), 162–168.
- (38) Allen, K. J. H.; Jiao, R.; Malo, M. E.; Frank, C.; Dadachova, E. Biodistribution of a Radiolabeled Antibody in Mice as an Approach to Evaluating Antibody Pharmacokinetics. *Pharmaceutics* **2018**, *10* (4).
- (39) Edelmann, M. R. Radiolabelling Small and Biomolecules for Tracking and Monitoring. *RSC Adv* **2022**, *12* (50), 32383–32400.
- (40) Ramos-Membrive, R.; Erhard, Á.; Luis de Redín, I.; Quincoces, G.; Collantes, M.; Ecay, M.; Irache, J. M.; Peñuelas, I. In Vivo SPECT-CT Imaging and Characterization of Technetium-99m-Labeled Bevacizumab-Loaded Human Serum Albumin Pegylated Nanoparticles. *J Drug Deliv Sci Technol* **2021**, *64*.
- (41) Myerson, J. W.; Patel, P. N.; Rubey, K. M.; Zamora, M. E.; Zaleski, M. H.; Habibi, N.; Walsh, L. R.; Lee, Y. W.; Luther, D. C.; Ferguson, L. T.; Marcos-Contreras, O. A.; Glassman, P. M.; Mazaleuskaya, L. L.; Johnston, I.; Hood, E. D.; Shuvaeva, T.; Wu, J.; Zhang, H. Y.; Gregory, J. V.; Kiseleva, R. Y.; Nong, J.; Grosser, T.; Greineder, C. F.; Mitragotri, S.; Worthen, G. S.; Rotello, V. M.; Lahann, J.; Muzykantov, V. R.; Brenner, J. S. Supramolecular Arrangement of Protein in Nanoparticle Structures Predicts Nanoparticle Tropism for Neutrophils in Acute Lung Inflammation. *Nat Nanotechnol* 2022, *17* (1), 86–97.

- (42) Johansson, U.; Macey, M. Pitfalls in the Use of Multicolour Flow Cytometry in Haematology. *J Clin Pathol* **2011**, *64* (7), 561–563.
- (43) Arppe, R.; Carro-Temboury, M. R.; Hempel, C.; Vosch, T.; Sørensen, T. J. Investigating Dye Performance and Crosstalk in Fluorescence Enabled Bioimaging Using a Model System. *PLoS One* **2017**, *12* (11), 1–17.
- (44) Arms, L.; Smith, D. W.; Flynn, J.; Palmer, W.; Martin, A.; Woldu, A.; Hua, S. Advantages and Limitations of Current Techniques for Analyzing the Biodistribution of Nanoparticles. *Front Pharmacol* **2018**, *9* (AUG), 1–17.
- (45) Simonsen, J. B.; Kromann, E. B. Pitfalls and Opportunities in Quantitative Fluorescence-Based Nanomedicine Studies A Commentary. *Journal of Controlled Release* **2021**, *335* (June), 660–667.
- (46) Nesterova, A. V.; Denisova, N. V. Pitfalls in the Path of Quantitative Assessment of the Severity of Oncological Lesions in Diagnostic Nuclear Medicine. *Technical Physics* **2022**, 67 (5), 401–410.
- (47) Burnum, K. E.; Tranguch, S.; Mi, D.; Daikoku, T.; Dey, S. K.; Caprioli, R. M. Imaging Mass Spectrometry Reveals Unique Protein Profiles during Embryo Implantation. *Endocrinology* **2008**, *149* (7), 3274–3278.
- (48) Yang, J.; Caprioli, R. M. Matrix Sublimation/Recrystallization for Imaging Proteins by Mass Spectrometry at High Spatial Resolution. *Anal. Chem.* **2011**, *83* (1), 5728-5734.
- (49) Stoeckli, M.; Chaurand, P.; Hallahan, D. E.; Caprioli, R. M. Imaging Mass Spectrometry: A New Technology for the Analysis of Protein Expression in Mammalian Tissues. *Nat Med* **2001**, *7* (4), 493–496.
- (50) Caprioli, R. M.; Farmer, T. B.; Gile, J. Molecular Imaging of Biological Samples: Localization of Peptides and Proteins Using MALDI-TOF MS. *Anal Chem* **1997**, *69* (23), 4751–4760.
- (51) Garza, K. Y.; Feider, C. L.; Klein, D. R.; Rosenberg, J. A.; Brodbelt, J. S.; Eberlin, L. S. Desorption Electrospray Ionization Mass Spectrometry Imaging of Proteins Directly from Biological Tissue Sections. *Anal Chem* **2018**, *90* (13), 7785–7789.
- (52) Cooper, H. J.; Hale, O. J. Native Mass Spectrometry Imaging of Proteins and Protein Complexes by Nano-Desi. *Anal Chem* **2021**, *93* (10), 4619–4627.
- (53) Yang, M.; Unsihuay, D.; Hu, H.; Nguele Meke, F.; Qu, Z.; Zhang, Z.-Y.; Laskin, J. Nano-DESI Mass Spectrometry Imaging of Proteoforms in Biological Tissues with High Spatial Resolution. *Anal Chem* **2023**.
- (54) Chang, Q.; Ornatsky, O. I.; Siddiqui, I.; Loboda, A.; Baranov, V. I.; Hedley, D. W. Imaging Mass Cytometry. *Cytometry Part A* **2017**, *91* (2), 160–169.
- (55) Elaldi, R.; Hemon, P.; Petti, L.; Cosson, E.; Desrues, B.; Sudaka, A.; Poissonnet, G.; Van Obberghen-Schilling, E.; Pers, J. O.; Braud, V. M.; Anjuère, F.; Meghraoui-Kheddar, A. High Dimensional Imaging Mass Cytometry Panel to Visualize the Tumor Immune Microenvironment Contexture. *Front Immunol* **2021**, *12* (April), 1–12.

- (56) Kakade, V. R.; Weiss, M.; Cantley, L. G. Using Imaging Mass Cytometry to Define Cell Identities and Interactions in Human Tissues. *Front Physiol* **2021**, *12* (December).
- (57) Baharlou, H.; Canete, N. P.; Cunningham, A. L.; Harman, A. N.; Patrick, E. Mass Cytometry Imaging for the Study of Human Diseases—Applications and Data Analysis Strategies. *Front Immunol* **2019**, *10* (November), 1–22.
- (58) Agrohia, D. K.; Wu, P.; Huynh, U.; Thayumanavan, S.; Vachet, R. W. Multiplexed Analysis of the Cellular Uptake of Polymeric Nanocarriers. *Anal Chem* **2022**, *94* (22), 7901–7908.
- (59) Lee, Y. W.; Luther, D. C.; Goswami, R.; Jeon, T.; Clark, V.; Elia, J.; Gopalakrishnan, S.; Rotello, V. M. Direct Cytosolic Delivery of Proteins through Coengineering of Proteins and Polymeric Delivery Vehicles. *J Am Chem Soc* **2020**, *142* (9), 4349–4355.
- (60) Luther, D. C.; Lee, Y. W.; Nagaraj, H.; Clark, V.; Jeon, T.; Goswami, R.; Gopalakrishnan, S.; Fedeli, S.; Jerome, W.; Elia, J. L.; Rotello, V. M. Cytosolic Protein Delivery Using Modular Biotin-Streptavidin Assembly of Nanocomposites. *ACS Nano* **2021**.
- (61) Goswami, R.; Lehot, V.; Çiçek, Y. A.; Nagaraj, H.; Jeon, T.; Nguyen, T.; Fedeli, S.; Rotello, V. M. Direct Cytosolic Delivery of Citraconylated Proteins. *Pharmaceutics* 2023, 15 (1), 1–10.
- (62) Luther, D. C.; Nagaraj, H.; Goswami, R.; Çiçek, Y. A.; Jeon, T.; Gopalakrishnan, S.; Rotello, V. M. Direct Cytosolic Delivery of Proteins Using Lyophilized and Reconstituted Polymer-Protein Assemblies. *Pharm Res* **2022**, *39* (6), 1197–1204.
- (63) Geng, Y.; Hardie, J.; Landis, R. F.; Mas-Rosario, J. A.; Chattopadhyay, A. N.; Keshri, P.; Sun, J.; Rizzo, E. M.; Gopalakrishnan, S.; Farkas, M. E.; Rotello, V. M. High-Content and High-Throughput Identification of Macrophage Polarization Phenotypes. *Chem Sci* 2020, 11 (31), 8231–8239.
- (64) Yokoyama, M.; Shiraishi, K. Stability Evaluation of Gd Chelates for Macromolecular MRI Contrast Agents. *Magnetic Resonance Materials in Physics, Biology and Medicine* **2020**, 33 (4), 527–536.
- (65) Ahrends, R.; Pieper, S.; Neumann, B.; Scheler, C.; Linscheid, M. W. Metal-Coded Affinity Tag Labeling: A Demonstration of Analytical Robustness and Suitability for Biological Applications. *Anal Chem* **2009**, *81* (6), 2176–2184.
- (66) Frenzel, T.; Lengsfeld, P.; Schirmer, H.; Hütter, J.; Weinmann, H. J. Stability of Gadolinium-Based Magnetic Resonance Imaging Contrast Agents in Human Serum at 37°C. *Invest Radiol* **2008**, *43* (12), 817–828.
- (67) Jantarat, T.; Lauterbach, J. D.; Doungchawee, J.; Agrohia, D. K.; Vachet, R. W. Quantitative Imaging of the Sub-Organ Distributions of Nanomaterials in Biological Tissues via Laser Ablation Inductively Coupled Plasma Mass Spectrometry. *Analyst* **2023**, 4479–4488.
- (68) Singh, A. P.; Guo, L.; Verma, A.; Wong, G. G. L.; Shah, D. K. A Cell-Level Systems PK-PD Model to Characterize in Vivo Efficacy of ADCs. *Pharmaceutics* **2019**, *11* (2), 1–18.
- (69) Yin, J.; Lang, T.; Cun, D.; Zheng, Z.; Huang, Y.; Yin, Q.; Yu, H. PH-Sensitive Nano-Complexes Overcome Drug Resistance and Inhibit Metastasis of Breast Cancer by Silencing Akt Expression. *Theranostics* **2017**, *7* (17).

- (70) Tencer, J.; Frick, I. M.; Öquist, B. W.; Alm, P.; Rippe, B. Size-Selectivity of the Glomerular Barrier to High Molecular Weight Proteins: Upper Size Limitations of Shunt Pathways. *Kidney Int* **1998**, *53* (3), 709–715.
- (71) Comper, W. D.; Glasgow, E. F. Charge Selectivity in Kidney Ultrafiltration. *Kidney Int* **1995**, 47 (5), 1242–1251.
- (72) Bohrer, M. P.; Deen, W. M.; Robertson, C. R.; Troy, J. L.; Brenner, B. M. Influence of Molecular Configuration on the Passage of Macromolecules across the Glomerular Capillary Wall. *Journal of General Physiology* **1979**, *74* (5), 583–593.
- (73) Zuckerman, J. E.; Choi, C. H. J.; Han, H.; Davis, M. E. Polycation-SiRNA Nanoparticles Can Disassemble at the Kidney Glomerular Basement Membrane. *Proc Natl Acad Sci U S A* 2012, 109 (8), 3137–3142.
- (74) Prossnitz, A. N.; Liu, G. W.; Eng, D. G.; Cheng, Y.; Pippin, J. W.; Lamm, R. J.; Ngambenjawong, C.; Shankland, S. J.; Pun, S. H. Glomerular Disease Augments Kidney Accumulation of Synthetic Anionic Polymers. *Transactions of the Annual Meeting of the Society for Biomaterials and the Annual International Biomaterials Symposium* **2019**, 40, 504.
- (75) Burke, R. S.; Pun, S. H. Extracellular Barriers to in Vivo PEI and PEGylated PEI Polyplex-Mediated Gene Delivery to the Liver. *Bioconjug Chem* **2008**, *19* (3), 693–704.
- (76) Merkel, O. M.; Librizzi, D.; Pfestroff, A.; Schurrat, T.; Buyens, K.; Sanders, N. N.; De Smedt, S. C.; Béhé, M.; Kissel, T. Stability of SiRNA Polyplexes from Poly(Ethylenimine) and Poly(Ethylenimine)-g-Poly(Ethylene Glycol) under in Vivo Conditions: Effects on Pharmacokinetics and Biodistribution Measured by Fluorescence Fluctuation Spectroscopy and Single Photon Emission Com. *Journal of Controlled Release* 2009, 138 (2), 148–159.
- (77) Kircheis, R.; Wightman, L.; Schreiber, A.; Robitza, B.; RÖssler, V.; Kursa, M.; Wagner, E. Polyethylenimine/DNA Complexes Shielded by Transferrin Target Gene Expression to Tumors after Systemic Application. *Gene Ther* **2001**, *8* (1), 28–40.
- (78) Mout, R.; Ray, M.; Tay, T.; Sasaki, K.; Yesilbag Tonga, G.; Rotello, V. M. General Strategy for Direct Cytosolic Protein Delivery via Protein-Nanoparticle Co-Engineering. *ACS Nano* **2017**, *11* (6), 6416–6421.
- (79) Mout, R.; Ray, M.; Yesilbag Tonga, G.; Lee, Y. W.; Tay, T.; Sasaki, K.; Rotello, V. M. Direct Cytosolic Delivery of CRISPR/Cas9-Ribonucleoprotein for Efficient Gene Editing. *ACS Nano* **2017**, *11* (3), 2452–2458.
- (80) Castellanos-García, L. J.; Gokhan Elci, S.; Vachet, R. W. Reconstruction, Analysis, and Segmentation of LA-ICP-MS Imaging Data Using Python for the Identification of Sub-Organ Regions in Tissues. *Analyst* **2020**, *145* (10), 3705–3712.